

# Development of a Subcell Based Modeling Approach for Modeling the Architecturally Dependent Impact Response of Triaxially Braided Polymer Matrix Composites

Christopher Sorini<sup>1</sup>, Aditi Chattopadhyay<sup>1</sup>, Robert K. Goldberg<sup>2</sup>, and Lee Kohlman<sup>2</sup>

<sup>1</sup>Arizona State University, Tempe, AZ, USA

<sup>2</sup>NASA Glenn Research Center, Cleveland, OH, USA

## Abstract

*Understanding the high velocity impact response of polymer matrix composites with complex architectures is critical to many aerospace applications, including engine fan blade containment systems where the structure must be able to completely contain fan blades in the event of a blade-out. Despite the benefits offered by these materials, the complex nature of textile composites presents a significant challenge for the prediction of deformation and damage under both quasi-static and impact loading conditions. The relatively large mesoscale repeating unit cell (in comparison to the size of structural components) causes the material to behave like a structure rather than a homogeneous material. Impact experiments conducted at NASA Glenn Research Center have shown the damage patterns to be a function of the underlying material architecture. Traditional computational techniques that involve modeling these materials using smeared, homogeneous, orthotropic material properties at the macroscale result in simulated damage patterns that are a function of the structural geometry, but not the material architecture. In order to preserve heterogeneity at the highest length scale in a robust yet computationally efficient manner and capture the architecturally dependent damage patterns, a previously-developed subcell modeling approach is utilized. This work discusses the implementation of the subcell methodology into the commercial transient dynamic finite element code LS-DYNA<sup>®</sup>. Verification and validation studies are also presented, including simulating the tensile response of straight sided and notched quasi-static coupons composed of a T700/PR520 triaxially braided (0°/60°/-60°) composite. Based on the results of the verification and validation studies, advantages and limitations of the methodology and plans for future work are discussed.*

## **Introduction**

Polymer matrix composites (PMCs) with complex textile architectures are increasingly being used by the aerospace industry in applications where impact resistance is critical, such as jet engine fan blade containment systems subjected to blade-out events. However, the complex nature of textile composites, particularly braided composites, presents a significant challenge for the prediction of the deformation and damage response of these structures, particularly under impact loading conditions. Experimental evidence has shown [1] that when these materials are subjected to impact, oftentimes the damage will propagate along fiber directions. This phenomenon is due to the relatively large repeating unit cell (RUC) in the braided composite as compared to the size of the composite structure [2]. Typically, modeling methodologies that have been developed to simulate the response of textile composites model the composite at the macroscopic scale as a smeared, orthotropic homogeneous material whereby only effective strength and stiffness properties are used [3]. However, when smeared homogeneous properties are used in numerical simulations to predict the initiation and propagation of damage, the damage patterns are merely functions of the structural geometry and the effects of the material architecture on the damage propagation are not properly accounted for [4].

To account for the effects of the composite architecture on the initiation and propagation of damage in a computationally efficient manner, a subcell-based approach has been developed in which the braided composite is approximated as a series of adjacent laminated composites [5-11]. The semi-analytical nature of this approach makes it both robust and computationally efficient. In this work, a critical evaluation and verification of this subcell methodology has been conducted. A number of simulations of straight-sided and notched tensile coupon tests have been conducted for a representative braided composite at a variety of different coupon orientations (0°, 30°, 60°, 90°). The results of the straight-sided coupon simulations are compared to those presented in Ref. 11 and the results of the notched coupon simulations are compared to experimental data.

## **Subcell Methodology**

The subcell methodology consists of identifying the braided composite RUC and discretizing it into a series of unique subcell regions depending on the presence of axial and/or braider tows or lack thereof. In Figure 1(a), the red arrow denotes the direction of axial tows whereas the blue arrows denote the directions of the bias/braider tows in a triaxial braid. The current version of the subcell model has been designed to analyze triaxially braided composites with a [0°/60°/-60°] fiber architecture. Future efforts will involve generalizing the methodology such that other textile composite architectures can be simulated. The dimensions of the RUC are illustrated in Figure 1(b) and the unique subcells for the T700/PR520 material system are shown in Figure 1(c). It can be seen that subcells A and C are the only subcells with axial tows (red) whereas subcells B and D contain only braider tows (grey/black). Each subcell is then discretized through the thickness into an approximation of unidirectional (UD) plies, as depicted in Figure 1(d). The subcell discretization method shown in Figure 1(d) is known as the absorbed matrix model (AMM) due to the fact that instead of explicitly modeling layers of matrix, the braider plies are assumed to be a homogenized representation of the braider tows and surrounding matrix regions [10, 11]. Following this method, subcells A and C are modeled as asymmetric composite laminates and subcells B and D are modeled as symmetric composite laminates. The asymmetry

of subcells A and C allows the model to capture tension-twist coupling and local out-of-plane deformations when a specimen is loaded in tension [11].

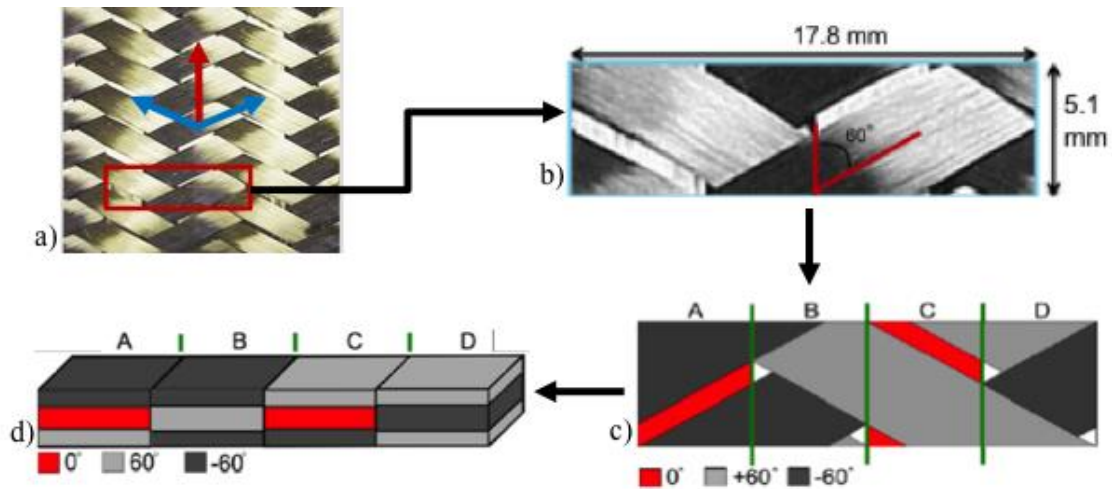


Figure 1. Discretization process to generate subcell model.

### Determination of Unidirectional Ply Thickness and Fiber Volume Fraction

Prior to the implementation of the subcell methodology into LS-DYNA [10], the appropriate geometric properties of the subcells must be determined. The approach described in Ref. 11 is used to determine the UD ply thicknesses and fiber volume fractions based on the geometric parameters presented in Table 1, which were determined in previous works by examining micrographs of the braided composite [5]. First the total volume of axial and/or braider fibers in subcells A/C and B/D are computed based on the fiber cross-sectional area, the number of fibers in each subcell, and the length of each of the axial/braider tows. The details of this process are described in Ref. 11. The lengths of the braider tows in subcells A/C and B/D are determined using the length, width, and height of the respective subcells and a straight-line assumption [8], in which the braider tows are approximated as a series of line segments; this is illustrated in Figure 2 and described in Ref. 8. Table 2 summarizes the calculated total volume of axial and braider fibers in each subcell.

**Table 1. Geometrical parameters used to determine unidirectional ply thicknesses and fiber volume fractions.**

Parameter	Description	Value
$W_A$	Width of subcell A	4.201 mm
$W_B$	Width of subcell B	4.765 mm
$H$	Height of RUC	0.56 mm
$V_{tow}$	Fiber volume fraction of axial tows (assumed)	80%
$n_a$	Number of fibers in axial tows	24k
$n_b$	Number of fibers in braider tows	12k
$d_a$	Diameter of axial tows	7 $\mu\text{m}$
$d_b$	Diameter of braider tows	7 $\mu\text{m}$
$L$	Length of unit cell	5.1 mm
$\Theta$	Braid angles	$\pm 60^\circ$

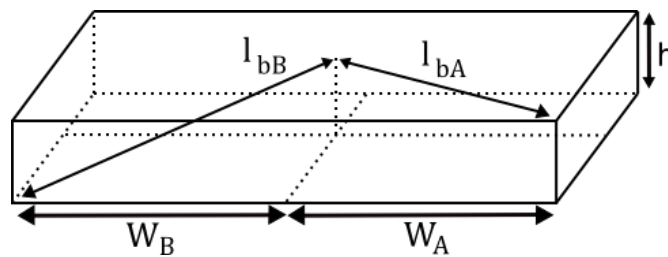


**Figure 2. Schematic of the straight-line model used to determine bias tow lengths.**

**Table 2. Total volume of axial and braider fibers in each subcell.**

Subcell	Total Volume of Bias Fibers ( $\text{m}^3$ )	Total Volume of Axial Fibers ( $\text{m}^3$ )
A/C	4.48E-09	4.71E-09
B/D	5.11E-09	0

The thicknesses of the UD plies in subcell A/C are computed based on an assumed axial tow fiber volume fraction of 80% as well as the length, width, and height of subcells A/C [5]. Although this is not mentioned in Ref. 11, the thicknesses of the UD layers of subcells B/D are determined based on the assumption that there is an equal amount of plus and minus  $60^\circ$  braider tows present in subcells B/D. The next step is to determine the fiber volume fractions of the braider tows in subcells A/C and B/D. This is done using the procedure described in Ref. 11. The results obtained agree with those in Ref. 11 and are shown in Table 3. It is important to note that there are three unique fiber volume fractions (37.5%, 73.3%, and 80%) corresponding to three unique ply regions.

**Table 3. Summary of calculated fiber volume fractions and thicknesses (\*shown as a percent of overall subcell thickness).**

Subcell A Layup	Braid Angle	Fiber Vf (%)	Thickness*
Braider tow	-60	73.3	0.255
Axial Tow	0	80	0.49
Braider Tow	60	73.3	0.255
Subcell B Layup	Braid Angle	Fiber Vf (%)	Thickness*
Braider tow	-60	37.5	0.25
Braider tow	60	37.5	0.5
Braider tow	-60	37.5	0.25

### Material Model

The commercial transient dynamic finite element code LS-DYNA [12] is used to model each of the subcells as a discrete laminated composite using Belytschko-Tsay composite shell elements and the LS-DYNA material model MAT\_058 (Laminated Composite Fabric). By modeling the RUC as four adjacent laminated composites that are individually homogenized through the thickness, but *not* homogenized in-plane, heterogeneity is preserved at the mesoscale (and higher length scales) and a balance between fidelity and computational efficiency is ensured. The unidirectional plies are represented by integration points stacked through the thickness of the shell elements using \*INTEGRATION\_SHELL cards to specify the layup and thickness of each layer and \*SECTION\_SHELL cards to specify the integration layer orientations. The RUC in LS-DYNA is shown in Figure 3.

MAT\_058 is a continuum damage mechanics model that utilizes the Hashin failure criterion in which the failure envelope is a function of longitudinal tension and compression, transverse tension and compression, and shear strengths [13, 14]. MAT\_058 uses exponential damage evolution in which damage parameters in the longitudinal, transverse, and shear directions control the degradation of the elastic properties and thus allow nonlinearity in the stress-strain response. Equation 1 shows the constitutive matrix as a function of damage in the longitudinal ( $\omega_{11}$ ), transverse ( $\omega_{22}$ ), and shear ( $\omega_{12}$ ) directions.

$$C(\omega) = \frac{1}{D} \begin{bmatrix} (1 - \omega_{11})E_{11} & (1 - \omega_{11})(1 - \omega_{22})v_{21}E_{22} & 0 \\ (1 - \omega_{11})(1 - \omega_{22})v_{12}E_{11} & (1 - \omega_{22})E_{22} & 0 \\ 0 & 0 & D(1 - \omega_{12})G \end{bmatrix} \quad (1)$$

$$\text{where } D = 1 - (1 - \omega_{11})(1 - \omega_{22})v_{12}v_{21}$$

The damage parameters range between 0 (undamaged) and 1 (fully damaged). Once a damage parameter reaches a value of unity in a particular direction, various stress limiting parameters allow the specification of a post-failure ‘plateau’ stress. In previous work [11] the tensile and compressive stress limiting parameters in the longitudinal direction, SLIMIT1 and SLIMC1, were both chosen to be 0.01 in order to prescribe brittle failure in the fiber direction. In this study, it was found that SLIMIT1 and SLIMC1 parameters of 0.3 and 0.1 work best to correlate to both the straight-sided and notched tension test data, which is discussed later. All other stress limiting parameters have been set to 1. MAT\_058 also allows special control of the maximum effective strain an element can experience before erosion (element deletion) occurs. In this study, no element erosion is used; any nonlinearity in the stress-strain curves is due solely to degradation of the elastic constants.

**Conference**

Since the Hashin failure criterion [13] is based on five stresses and the corresponding strain values, a total of ten strength (and corresponding strain) values need to be specified for each \*MAT\_58 material definition. There are a total of three material definitions; one for each unique UD ply region/fiber volume fraction (see Table 3), which means each model requires 30 parameters to characterize the strength of the material (note this excludes moduli, stress limiting parameters, etc.). The next section discusses the process for populating the required input parameters of \*MAT\_058 (strength and stiffness) using top-down unit cell and bottom-up micromechanics techniques.

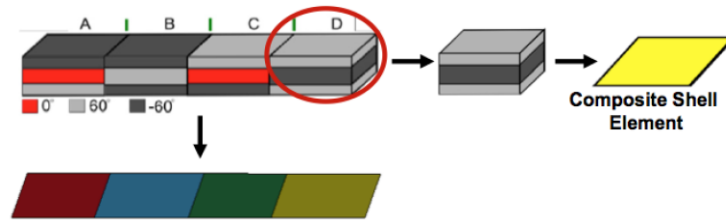


Figure 3. Schematic illustrating how the subcell methodology is implemented into LS-DYNA.

**Bottom-Up Micromechanics Approach to Determine Unidirectional Ply Stiffness, Transverse Tensile Strength, and Shear Strength**

Due to the processing methods used for braided composites, equivalent UD coupons for physical testing cannot be manufactured; therefore a bottom-up micromechanics approach is utilized to determine the stiffness properties of the three unique UD ply regions based on the fiber volume fraction of the respective region and constituent properties, which can be seen in Table 4. NASA’s MAC/GMC software [15] is employed to compute the UD ply stiffness properties. MAC/GMC is a Micromechanics Analysis Code developed at NASA based on the Generalized Method of Cells [16] and can predict the elastic and inelastic thermo-mechanical response of composites. The resulting effective UD stiffness properties for the three unique ply regions are shown in Table 5.

Table 4. Elastic properties of the T700 fibers and PR520 matrix.

Material	Density (g-cm <sup>3</sup> )	E <sub>11</sub> (GPa)	E <sub>22</sub> (GPa)	G <sub>12</sub> (GPa)	v <sub>12</sub>
T700 (Fiber)	1.8	230	15	27	0.2
PR520 (Matrix)	1.25	4	4	1.44	0.38

Table 5. Effective ply stiffness properties for three unique subcell regions.

Description	UD Vf	E <sub>11</sub> (GPa)	E <sub>22</sub> (GPa)	E <sub>33</sub> (GPa)	G <sub>23</sub> (GPa)	G <sub>13</sub> (GPa)	G <sub>12</sub> (GPa)	v <sub>12</sub>
B-Braider	37.50%	88.5	6.22	6.22	2.04	2.86	2.6	0.3
A-Braider	73.30%	169.5	9.9	9.9	3.4	8.68	7	0.23
A-Axial	80%	184.7	10.9	10.9	3.39	10.88	6	0.24

MAC/GMC is utilized in conjunction with a nonlinear, strain rate dependent polymer constitutive model [17], which incorporates hydrostatic stress effects to create stress-strain curves used to determine the MAT\_058 inputs for the transverse tensile and shear strengths and the corresponding failure strains for the three unique UD ply regions. This process is discussed in detail in Ref. 11. The transverse tensile strengths and corresponding failure strains were determined from the plots in Figure 4(a) and are denoted “LT” and “E22T” in Table 6. The shear strength and the stress at the first slightly nonlinear part of the stress-strain curves and corresponding strains were determined from the graphs in Figure 4(b) and are denoted “SC”, “TAU1”, “GMS”, and “GAMMA1”, respectively, in Table 7.

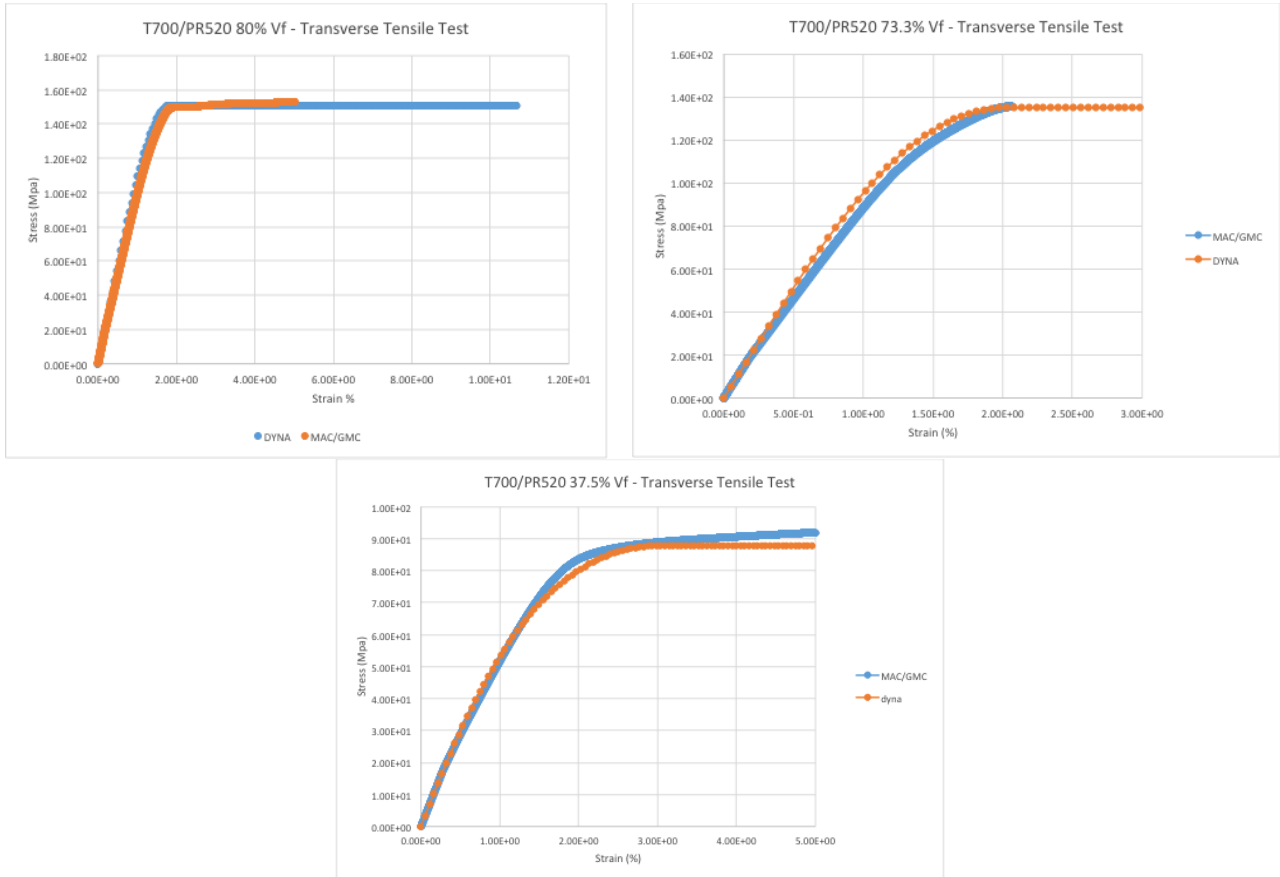
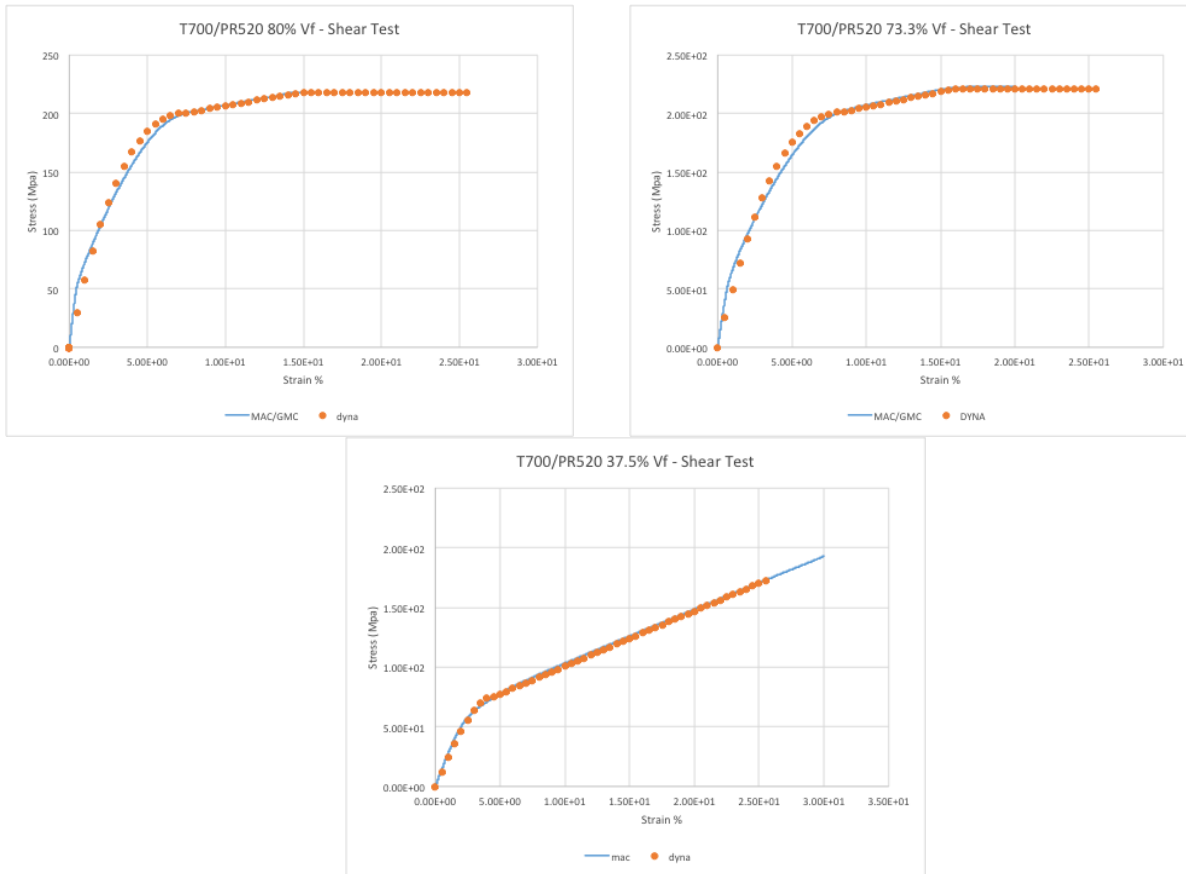


Figure 4(a). Stress-strain curves for transverse tension simulations for the three unique UD ply regions, both generated in MAC/GMC and in LS-DYNA.



**Figure 4(b). Stress-strain curves for in-plane shear simulations for the three unique UD ply regions, both generated in MAC/GMC and in LS-DYNA.**

## **Top Down Unit Cell Approach to Determine Longitudinal Tensile and Compressive Ply Strengths**

The longitudinal tensile and compressive strengths of the axial UD plies (with 80% fiber volume fraction) are determined utilizing the top-down unit cell approach discussed in Ref. 11. Using this approach, the strength properties are “backed-out” based on coupon-level test data. For example, in order to determine the longitudinal tensile strength of the axial plies, a coupon-level test that exhibits a tensile failure of the axial plies needs to be identified. The failure mode of the straight-sided axial tension tests was identified to be a tensile failure of the axial tows (parallel to the applied loading) [18]. A single RUC was then modeled in LS-DYNA and loaded to the macroscopic failure strength. The longitudinal stress in the integration point representing the axial ply was determined and set to be the ultimate longitudinal strength. The same unit cell approach is used to determine the longitudinal compressive strengths of the bias tows. The longitudinal tensile strengths of the bias plies (fiber volume fractions of 73.3% and 37.5%) are determined by making the assumption that the failure strain is equal to that of the axial plies (approximately 1.9%). The modulus is then used to determine the failure strength. Due to the fact that transverse compressive failure of the bias tows was not a failure mode observed in experiments, the transverse compressive strengths of the bias tow ply regions (fiber volume fractions of 73.3% and 37.5%) are assumed equal to the in-plane shear strengths. Both of the aforementioned assumptions are also made in Ref. 11. The strengths and corresponding strains used in the simulations are summarized in Tables 6 and 7.

Table 6. Summary of strengths for the three unique UD ply regions.

	UD Ply Strength (MPa)					
	XT	XC	YT	YC	SC	TAU1
Axial Plies	3599	1379	151	218	218	50
A/C Braider Plies	1648	696	135	221	221	201
B/D Braider Plies	938	403	87.7	193.4	193.4	75

Table 7. Summary of failure strains for the three unique UD ply regions.

	UD Failure Strain					
	E11T	E11C	E22T	E22C	GMS	GAMMA1
Axial Plies	0.0195	0.0075	0.0182	0.0191	0.1475	0.0750
A/C Braider Plies	0.0195	0.0045	0.0200	0.0211	0.1600	0.0840
B/D Braider Plies	0.0195	0.0041	0.0300	0.0295	0.3000	0.0450

## Straight-Sided Coupon Simulation Results

The material system considered in this work is a T700/PR520 2D triaxially braided ( $0^\circ/60^\circ/-60^\circ$ ) composite, which has 24K carbon fiber tows in the axial ( $0^\circ$ ) direction and 12K carbon fiber tows in the bias/braider ( $\pm 60^\circ$  with respect to the axial tows) directions. All experimental testing was carried out at NASA Glenn Research Center using a MTS servo-hydraulic load frame under displacement control at a displacement rate of 0.05 inches per minute. Note that the applied loading is in the vertical direction in all figures that follow (both experimental and simulated).

The coupon geometry for the  $0^\circ$ ,  $30^\circ$ ,  $60^\circ$ , and  $90^\circ$  straight-sided off-axis tension simulations are shown in Figure 5. The directions of the axial and bias tows are denoted by the red and blue arrows, respectively. Note that in the finite element models, only the axial tows are continuous. In previous subcell research [10, 11], the dimensions of the elements had physical significance. However, in order to create the notched coupon geometry (discussed later), a smaller mesh size needs to be used for the entire coupon. If smaller elements were only used near the notch, strain would localize in these elements due to mesh dependence (strain localization) issues with continuum damage mechanics models [19]. For consistency, the straight-sided coupon simulations were also conducted with the same mesh sizes used in the notched coupon simulations.

In previous works [10, 11], it was found that the transverse ( $90^\circ$ ) modulus was better captured when modeling with six layers of shell elements through the coupon thickness, each with 3 integration layers. However, preliminary impact simulations revealed that models with multiple layers of shell elements through the thickness yielded nonphysical impact response. Since the final goal is to simulate flat panel impact tests, all models in this study use a single shell element through the thickness with 18 integration points.

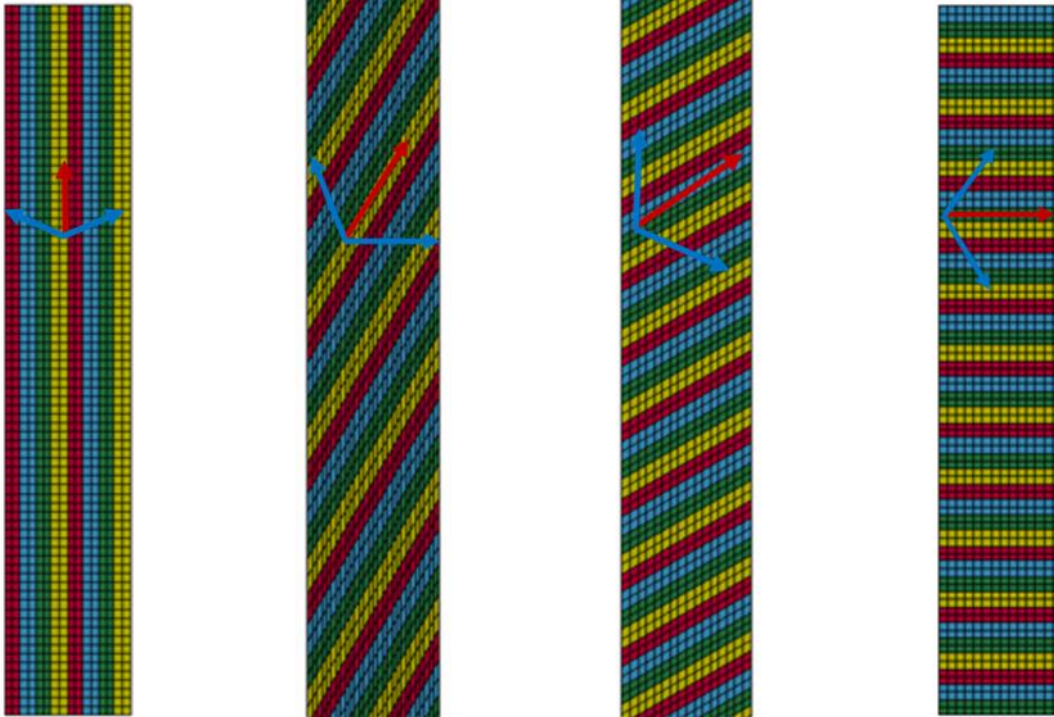
Conference

Figure 5. Geometry for 0°, 30°, 60°, and 90° straight-sided coupons created in LS-DYNA.

The stress-strain curve for the 0° axial tension simulation as well as the experimental data can be seen in Figure 6(a). The predicted strength of 904 MPa correlates well to the experimentally observed strength of 984 MPa, however the modulus value from the simulation is higher than that of the experiment. This increase in modulus was observed in changing from six layers of shell elements through the thickness, each with 3 integration layers, to one layer of shell elements through the thickness with 18 integration layers. The predicted failure mode of the 0° coupon is a tensile failure of the axial tows, which is in agreement with the observed experimental failure mode. This failure occurred near the grips in the simulation, which may be partially due to boundary conditions. Figure 7 shows the axial tows carrying majority of the applied loading prior to failure. The maximum stress value of 5.22e5 psi, which is equal to the ultimate strength (XT) specified for the axial tows (3599 MPa), occurs in the axial tows near the grips.

The stress-strain curve for the 30° off-axis tension simulation as well as the experimental data can be seen in Figure 6(b). The strength predicted by the simulation (approximately 580 MPa) is slightly higher than the two experimentally measured strengths of 450 MPa and 520 MPa. It should be noted that in Ref. 11, the predicted strength of the 30° straight-sided coupon is approximately 500 MPa. The difference can be attributed to using one layer of shell elements through the thickness instead of six. Despite the discrepancy in predicted strength from the experimental values, the predicted failure mode agrees with experiments and the results of Ref. 11. This predicted failure mode is a compressive failure of the bias tows oriented perpendicular to the loading direction, which are in compression due to Poisson's effect. The damage in the simulation initiates in the gage section of the coupon then progresses in the direction of the axial tows.

Both the predicted strength and modulus of the 60° coupon are in good agreement with experimental data, as seen in Figure 6(c). In the simulation, damage initiates at the edge of the coupon near the grips and progresses to the other side of the coupon in the direction of the axial

tows. This is in good agreement with the experimental failure mode, as shown in Figure 8 and explained in more detail in Ref. 11. The stress-strain curve for the 90° transverse tension coupon simulation is shown in Figure 6(d). The results are in good agreement with the results obtained in Ref. 11, however the predicted strength, modulus, and failure mode does not agree with experiments. The simulation predicts a tensile failure of the bias tows whereas an edge initiated shear failure was observed in experiments, possibly due to edge damage induced from cutting the coupons [18].

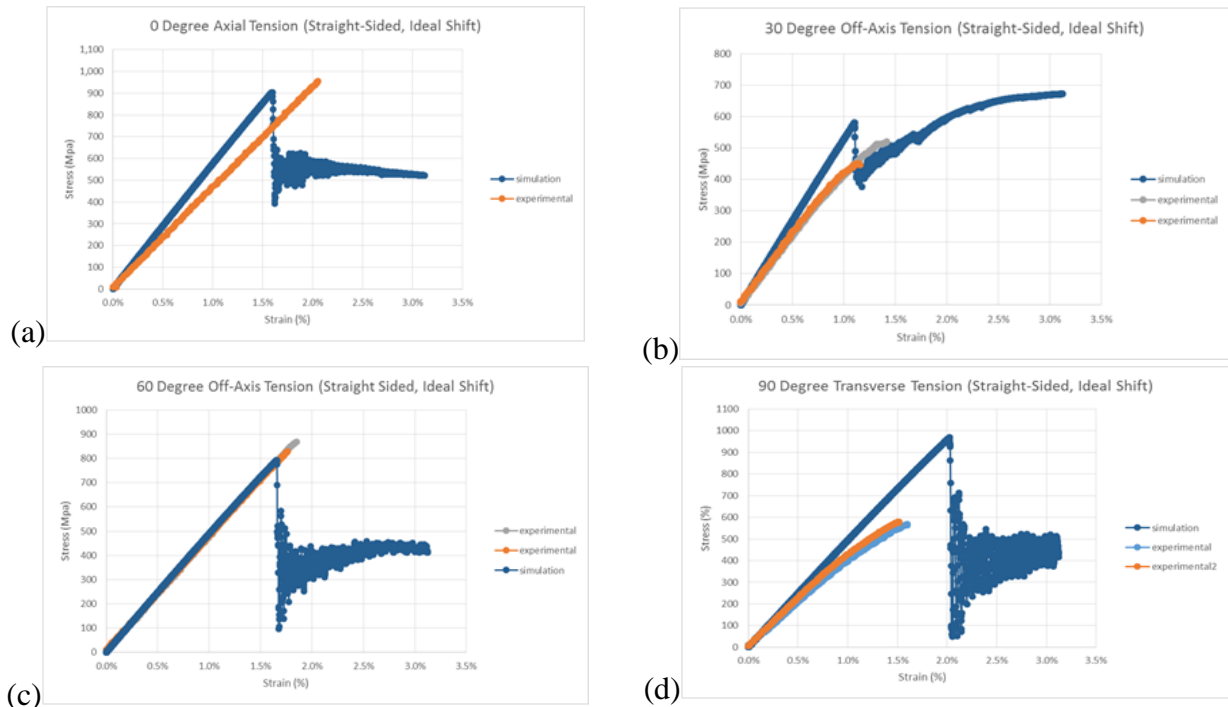


Figure 6. Stress-strain curves for straight-sided coupon simulations; (a) 0° axial tension; (b) 30° off-axis tension; (c) 60° off-axis tension; (d) 90° transverse tension.

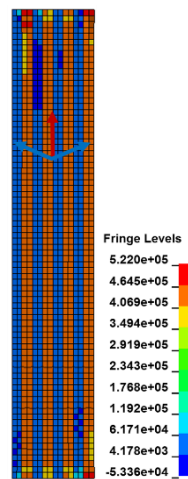


Figure 7. Contours of stress in the axial tow direction (fringe levels are in psi).

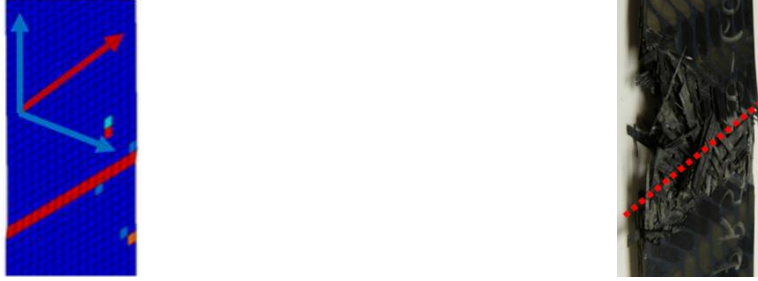
**Conference**

Figure 8. LS-DYNA simulation of 60° off-axis tension simulation; simulation (left) and experiment (right) both show a tensile failure of the bias tows oriented parallel to the applied loading and a failure path in the direction of the axial tows.

### Notched Coupon Experimental Failure Modes

Notched transverse tension tests were initially performed to mitigate edge effects observed in the straight-sided transverse tension experiment [18]. For completeness, the failure modes of notched tension tests conducted for various off-axis angles (30°, 45°, 60°, and 90°) with respect to the axial tows were studied. Note that only the 0°, 30°, 60°, and 90° notched coupon results will be discussed. The 0° notched axial tension coupon, shown in Figure 9(a), failed due to a tensile failure of the axial tows oriented parallel to the applied loading; the same failure mode was identified in the straight-sided axial tension experiment. Though both the straight sided and notched axial tension experiments exhibit the same failure mode, the ultimate strength of the notched coupon is lower. Kohlman [18] attributes this decrease in ultimate strength to early failure of the local axial tows near the notch tip(s) due to stress concentrations. The 30° notched off-axis tension coupon failed due to a tensile failure of the -60° bias tows (the bias tows that are not oriented perpendicular to the applied loading). Notice that in Figure 9(b), the top half (above the notch) of the 30° coupon has shifted to the right. It is hypothesized that this is caused by the load transferring to the axial tows after the failure of the bias tows, causing them to align with the load direction and the top of the coupon to shift. Note that transverse tow splits can be seen in the bias tows oriented perpendicular to the applied loading. The 60° notched off axis tension coupon failed due to a tensile failure of the bias tows along the loading direction. As shown in Figure 9(c), damage initiates at the notch tip and propagates in the direction of the axial tows. It can be seen that the bias tows break at the points in which they undulate underneath the axial tows; there are stress concentrations at the point of undulation, but the tough PR520 resin will not allow debonding, so the bias tows fail. The 90° transverse tension coupon failed due to a tensile failure of the bias tows, just as they were designed to do [18]. It can be seen that majority of the damage is localized in between the notch tips.

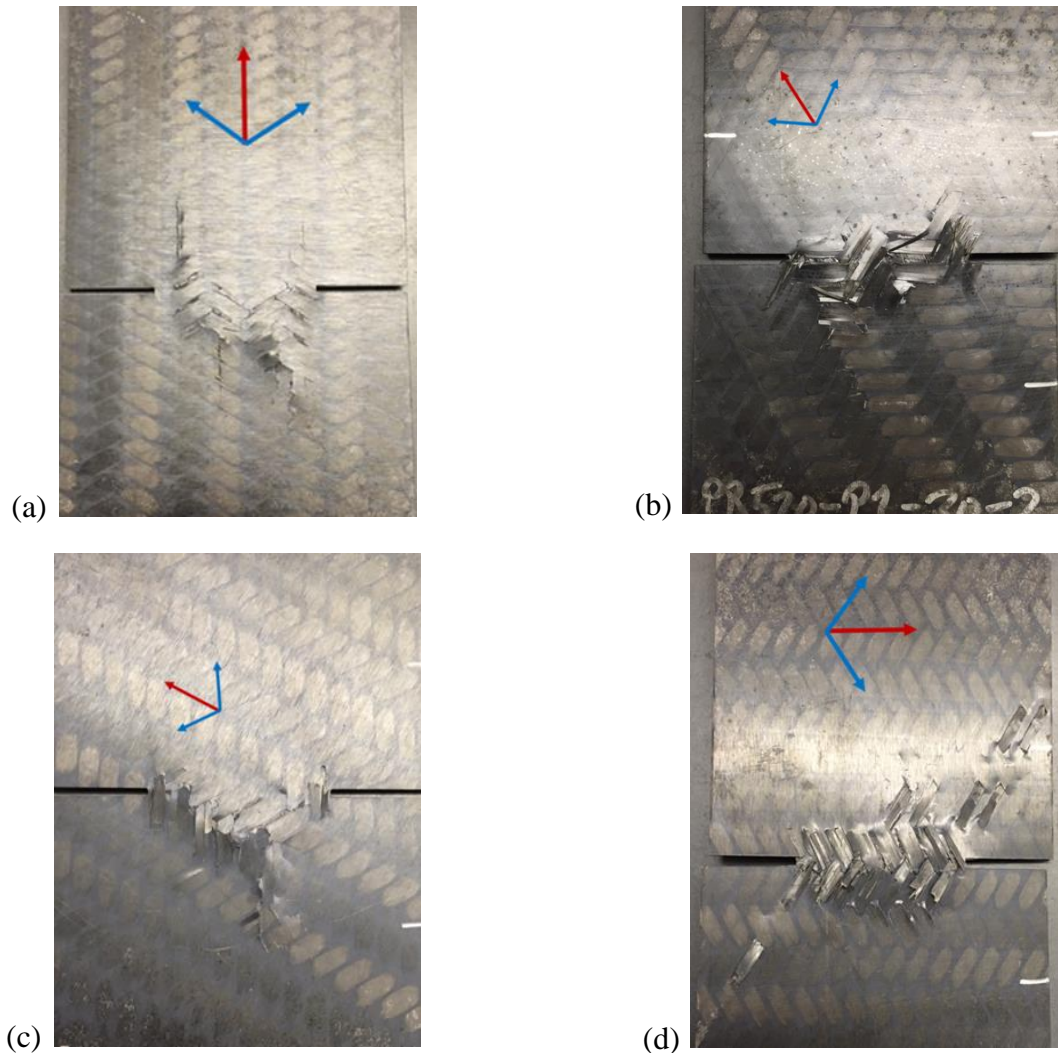


Figure 9. Failed notched coupons; (a) 0°; (b) 30°; (c) 60°; (d) 90°.

### Notched Coupon Simulation Results

The predicted failure modes of the notched coupons are discussed in this section. Note that the simulations have been conducted using the same material properties used in the straight-sided simulations. The stress-strain curves for the 0°, 30°, 60°, and 90° notched coupon simulations are shown in Figure 10 (a)-(d). The predicted strength and modulus of the 0° notched tension coupon are 770 MPa and 73 GPa, respectively. In the simulation, damage initiates in the axial tows near the notch tips (parallel to the applied loading) at around 0.8% strain. The damage in the axial tows then progresses from notch tip to notch tip. The axial tows closest to the notch tip fail in tension first, which causes majority of the load to be transferred to the remaining axial tows followed by subsequent tensile failure. A contour plot of the maximum value of damage in the (local) longitudinal direction immediately following the global load drop can be seen in Figure 11. Majority of the damage corresponds to the axial tows, though some damage in the bias tows is observed.

The predicted strength and modulus of the 30° notched tension coupon are 903 MPa and 66 GPa, respectively. Damage in the simulation initiates in the -60° bias tows (the bias tows that

**Conference**

are not oriented perpendicular to the applied loading) at the notch tips at approximately 0.5% strain. These tows are in tension. The damage then progresses in the direction of the axial tows, as shown in Figure 12. Note that the contour plot in Figure 12 shows the *maximum* value of damage in the (local) longitudinal direction, so the fully damaged (red) elements are not necessarily in the same integration layer (and thus do not necessarily correspond to the same tow). In fact, the damage corresponds to both  $-60^\circ$  bias and  $0^\circ$  axial tows in tension as well as  $+60^\circ$  bias tows (bias tows that are oriented perpendicular to the applied loading) in compression due to Poisson's effect. At approximately 1.7% strain (just prior to failure), damage in the axial tows progresses from the left notch tip to the right notch tip. The load drop in the simulation does not occur until all the axial tows between the notch tips have failed in tension. Thus, the predicted failure mode is a combined tensile failure of the  $-60^\circ$  bias tows and the axial tows. Note that this slightly differs from the experimentally observed failure mode, which was identified as a tensile failure of the bias tows. Figure 13 shows a contour plot of the maximum value of damage in the (local) longitudinal direction just after failure.

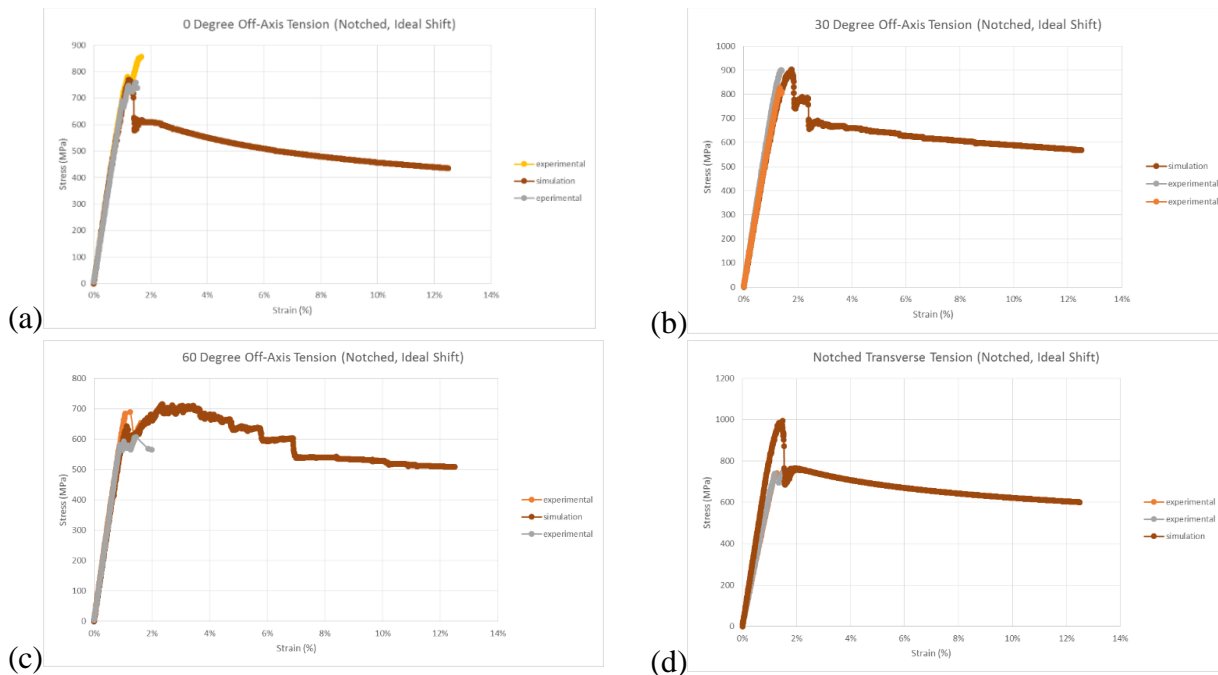


**Figure 10. Stress-strain curves for notched coupon simulations; (a)  $0^\circ$  axial tension; (b)  $30^\circ$  off-axis tension; (c)  $60^\circ$  off-axis tension; (d)  $90^\circ$  transverse tension**

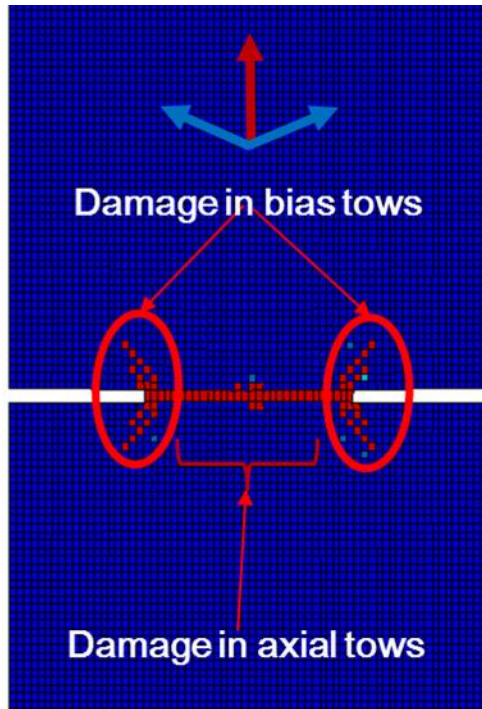


Figure 11. Contour plot of the maximum value of (local) longitudinal damage in 0° notched coupon just after the global load drop.

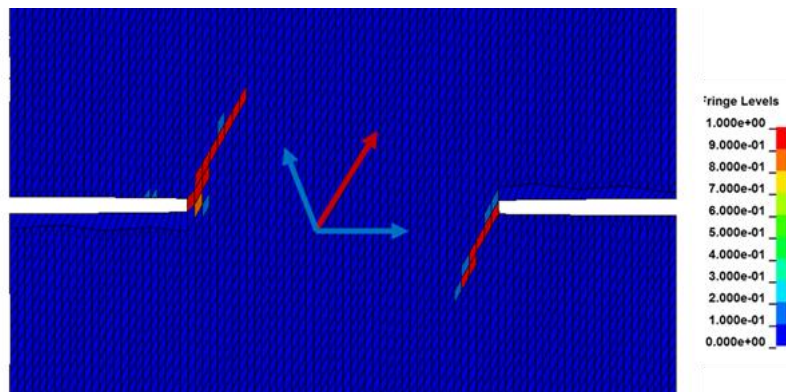
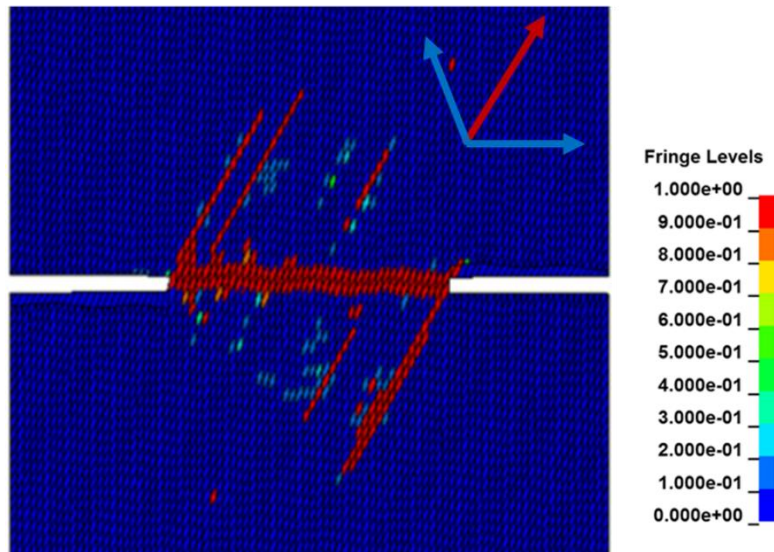


Figure 12. Contour plot showing the maximum value of (local) longitudinal damage in the 30° notched coupon; damage initiates at the notch tips and progresses in the direction of the axial tows.



**Figure 13. Contour plot of the maximum value of (local) longitudinal damage in the 30° coupon just after failure.**

The predicted strength and modulus for the 60° off axis notched coupon are 642 MPa and 64 GPa, respectively. Damage initiates at the notch tip in the bias tows that are aligned with the applied loading and progresses in the direction of the axial tows. Figure 14 shows contours of the maximum value of (local) longitudinal damage just after the load drop. This damage is only visible on the integration layers that correspond to -60° bias tows. Thus, the predicted failure mode is a tensile failure of the bias tows oriented parallel to the applied loading, which agrees with the experimental failure mode. It should be noted that after the initial load drop, the 60° coupon simulation continued to take load, as can be seen in Figure 10(c). The predicted strength and modulus of the 90° notched transverse tension coupon are 994 MPa and 84 GPa, respectively. Damage initiates in the bias tows (both +/- 60°) at the notch tips at about 1.1% strain and progresses in the direction of the axial tows (from notch tip to notch tip). The simulated damage pattern just after the load drop is highly localized between the notch tips and can be seen in Figure 15. All the red (fully damaged) elements in Figure 15 correspond to bias tows. Thus, the predicted failure mode is a tensile failure of the bias tows, which agrees well with the experiment.

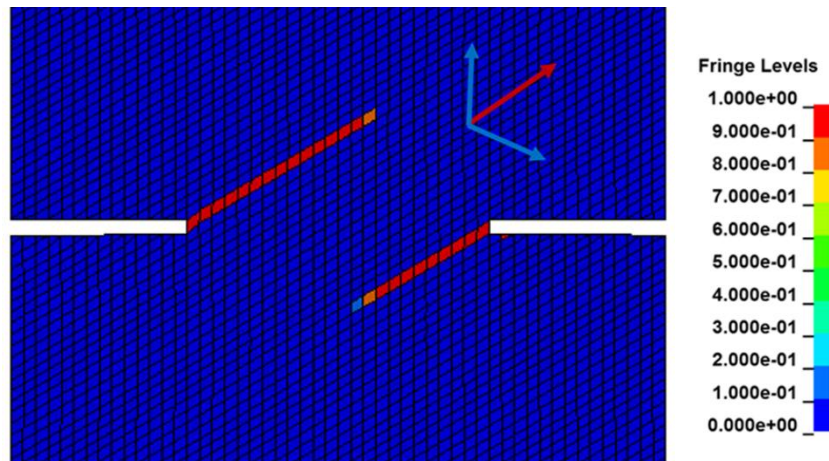


Figure 14. Contour plot of max. value of (local) longitudinal damage in the 60° notched coupon just after the load drop; all damaged (red) elements correspond to bias tows oriented parallel to the applied loading, which are in tension.

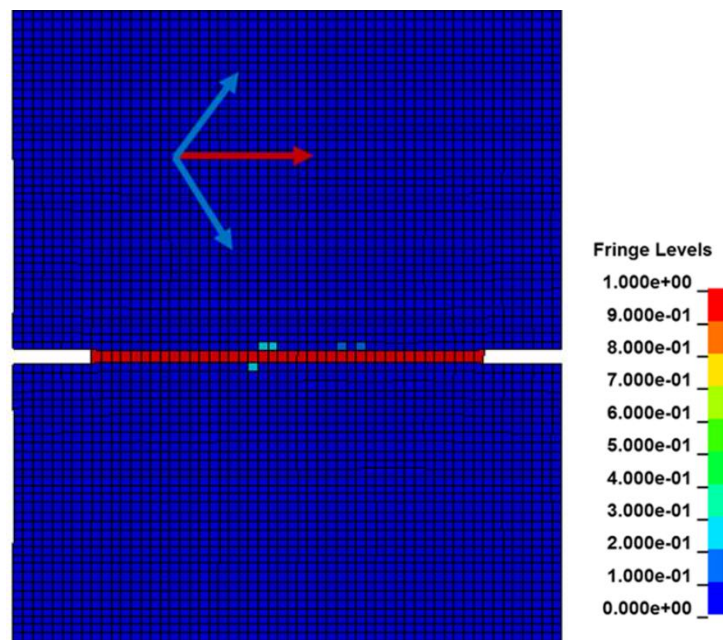


Figure 15. Contour plot of maximum value of (local) longitudinal damage just after global load drop; fully damaged (red) elements correspond to bias tows that have failed in tension.

## Conclusion

A previously-developed semi-analytical subcell based modeling approach has been utilized to investigate the tensile strength and failure mechanisms of a PR520/T700 triaxially braided (0°/60°/-60°) material system. Straight-sided and notched coupons were loaded in tension at a variety of off-axis angles (0°, 30°, 60°, and 90°) with respect to the axial tows. Model parameters (strengths and stiffness properties) were obtained using top-down unit cell and bottom-up micromechanics techniques. The predicted strength and failure modes of the 0°, 30°, and 60° straight-sided coupon simulations agree well with experiments. However, the strength and failure mode of the straight-sided transverse tension simulation does not agree with the experiments because the edge initiated shear failure observed in experiments is not taken into account in the numerical model. The notched coupon simulations also agree well with

**Conference**

experiments in terms of strength and failure mode, though the strength was slightly over predicted for the 90° loading direction case. The results of this research will be used in the development of a generalized design and analysis methodology for advanced PMCs, reducing the certification timeline for advanced composite materials, a goal of NASA's Advanced Composites Project (ACP). Future work includes conducting flat panel impact simulations as well as generalizing the subcell methodology such that it can be applied to various textile architectures.

## References

- [1] Pereira, J. M., et al., "Experimental Techniques for Evaluating the Effects of Aging on Impact and High Strain Rate Properties of Triaxial Braided Composite Materials," NASA TM-216763, 2010.
- [2] Littell, J. (2008). "The experimental and analytical characterization of the macromechanical response for triaxial braided composite materials" (Doctoral dissertation, The University of Akron).
- [3] Tanov, R., & Tabiei, A. (2001). "Computationally efficient micromechanical models for woven fabric composite elastic moduli". *Journal of Applied Mechanics*, 68(4), 553-560.
- [4] Roberts, G. D., Goldberg, R. K., Biniendak, W. K., Arnold, W. A., Littell, J. D., & Kohlman, L. W. (2009). "Characterization of triaxial braided composite material properties for impact simulation".
- [5] Blinzler, B. J., "Systematic approach to simulating impact for triaxially braided composites," Ph.D. Dissertation, Department of Civil Engineering, University of Akron, Akron, OH, 2012.
- [6] Li, X., Binienda W. K., and Littell, J. D., "Methodology for impact modeling of triaxial braided composites using shell elements." *Journal of Aerospace Engineering* 22.3 (2009): 310-317.
- [7] Cheng, J., and Binienda, W. K., "Simplified braiding through integration points model for triaxially braided composites." *Journal of Aerospace Engineering* 21.3 (2008): 152-161.
- [8] Xiao, X., et al. "Strength prediction of a triaxially braided composite." *Composites Part A: Applied Science and Manufacturing* 42.8 (2011): 1000-1006.
- [9] Goldberg, R. K., Blinzler, B. J., and Binienda, W. K., "Modification of a Macromechanical Finite Element-Based Model for Impact Analysis of Triaxially Braided Composites." *Journal of Aerospace Engineering* (2011).
- [10] Cater, C. R., et al. "Single Ply and Multi-Ply Braided Composite Response Predictions Using Modified Subcell Approach." *Journal of Aerospace Engineering* (2014): 04014117. DOI: 10.1061/(ASCE)AS.1943-5525.0000445.
- [11] Cater, C. R., Xiao, X., Goldberg, R. K., & Kohlman, L. W. "Experimental and Numerical Analysis of Triaxially Braided Composites Utilizing a Modified Subcell Modeling Approach," NASA TM-18814, 2015.
- [12] Hallquist, J. Q., "LS-DYNA<sup>®</sup> Keyword User's Manual," Volume II Material Models, Version 971, Livermore Software Technology Company, Livermore, CA, 2006.
- [13] Hashin, Z. "Failure criteria for unidirectional fiber composites." *Journal of Applied Mechanics* 47.2 (1980): 329-334.
- [14] Matzenmiller, A. L. J. T. R., Lubliner, J., and Taylor, R. L., "A constitutive model for anisotropic damage in fiber-composites." *Mechanics of materials* 20.2 (1995): 125-152.
- [15] Bednarczyk, B. A. and Arnold, S. M., "MAC/GMC 4.0 User's Manual—Keywords Manual," NASA TM-212077, 2002.
- [16] Paley, M., and Aboudi, J., "Micromechanical analysis of composites by the generalized cells model." *Mechanics of Materials* 14.2 (1992): 127-139.
- [17] Goldberg, R. K., Roberts, G. D., and Gilat A., "Implementation of an associative flow rule including hydrostatic stress effects into the high strain rate deformation analysis of polymer matrix composites." *Journal of Aerospace Engineering* 18.1 (2003): 18-27.
- [18] Kohlman, L. W., "Evaluation of test methods for triaxial braid composites and the development of a large multiaxial test frame for validation using braided tube specimens", Ph.D. Dissertation, Department of Civil Engineering, University of Akron, Akron, OH, 2012.
- [19] Pijaudier-Cabot, G., & Bazant, Z. P. (1987). Nonlocal damage theory. *Journal of Engineering Mechanics*, 113(10), 1512-1533.